A porous viscoelastic model for the cell cytoskeleton

Calina A. Copos,¹
Department of Mathematics,
University of California Davis, Davis, CA 95616, USA

Robert D. Guy
Department of Mathematics,
University of California Davis, Davis, CA 95616, USA

¹Corresponding author

Abstract

The immersed boundary method is a widely used mixed Eulerian/Lagrangian framework for simulating the motion of elastic structures immersed in viscous fluids. In this work, we consider a poroelastic immersed boundary method in which a fluid permeates a porous, elastic structure of negligible volume fraction, and extend this method to include stress relaxation of the material. The porous viscoelastic method presented here is validated for a prescribed oscillatory shear and for an expansion driven by the motion at the boundary of a circular material by comparing numerical solutions to an analytical solution of the Maxwell model for viscoelasticity. Finally, an application of the modelling framework to cell biology is provided: passage of a cell through a microfluidic channel. We demonstrate that the rheology of the cell cytoplasm is important for capturing the transit time through a narrow channel in the presence of a pressure drop in the extracellular fluid.

Contents

1	Introduction		
2	Mat 2.1	hematical framework Formulation of poroelasticity	4 4
	2.2	Formulation for viscoelasticity	7 8
3	Rhe	ological validations	10
	3.1	Small amplitude oscillatory shear test 3.1.1 Numerical validation	10 11 12 13 14 15
4	An a	application: Simulation of a cell in a microfluidic channel	17
-	4.1 4.2 4.3 4.4	Model of the cell	17 19 20 21
5	Con	clusions	22
A	Solu	tion to the linearized Maxwell model for a linear expansion	27

1 Introduction

Fluid-structure interaction problems are ubiquitous in biological and physical systems. The immersed boundary method [26] provides a computational framework that couples the dynamics of the immersed structure with the viscous, incompressible fluid. It has been applied to many problems such as blood flow in the heart [26], flagellar swimming [7, 9], and biofilm processes [10]. Recently, the immersed boundary method has been adapted to simulate poroelastic media in which the fluid permeates a porous, elastic structure of small volume fraction that moves with its own velocity field [30]. This variant has been applied to study biological systems such as crawling of the *Physarum* amoeba [19] and cellular blebbing [31]. However, the method has been limited to elastic networks, but many biological materials, such as the cell cytoplasm [12] and collagen gels [24], exhibit stress relaxation due to the rearrangement of the structure on timescales longer than minutes. In this paper, we are motivated by the time-evolving rheology of the cell cytoplasm and how its material properties affect cell locomotion in confined environments.

The cellular cytoplasm is a mixture of organelles, the cytosol, and the cytoskeleton. The cytosol is the liquid portion of the cytoplasm and it consists of water, ions, and dissolved molecules. The cytoskeleton is a dynamic network of filamentous proteins, including actin filaments, microtubules, and intermediate filaments, that give the cell its shape and ability to move. However, the cytoskeletal network is not a simple linear, elastic solid; it can exhibit highly non-linear elasticity and dynamics driven by ATP-dependent processes [12]. The cytoplasm has been modelled on the continuum level as an elastic material, viscoelastic material, porous gel, and viscous fluid [1, 13, 23, 31]. The appropriate mechanical model to describe this complex active bio-structure depends on the timescale and relevant cellular processes under consideration. Notably, the actin filaments involved in cell locomotion polymerise, depolymerise, and reorganise on a timescale of minutes. Therefore, the actin network behaves like an elastic solid on timescales of seconds, but a viscous fluid on timescales longer than minutes. On intermediate timescales, the actin network behaves like a elastic material that exhibits stress relaxation.

Motivated by the rearrangement of the cytoskeletal network, the contribution of this work is to incorporate a model for stress relaxation in our existing framework for simulating porous elastic structures immersed in a viscous fluid. The modelling framework in Strychalski et al. [30] is an extension of the immersed boundary method for simulating poroelastic media immersed in incompressible viscous fluid; the fluid dynamics equations are solved on a fixed Eulerian grid, while the structure forces are solved on a moving Lagrangian framework and transfer operators are used for the communication between grids [26]. The method for computing elastic forces on the material is reviewed and extended to include stress relaxation of the material. Once these material forces are accounted for, one can solve the equations of fluid motion in different ways. Rather than employ the framework of the immersed boundary method, here we use the grid-free method of regularised Stokeslets [6], that constructs the flow field due to a distribution of regularised forces.

There are other methods for modelling moving and deforming viscoelastic materials, such as the mixed Eulerian/Lagrangian methods which involve mapping elastic quantities between coordinate systems repeatedly [11, 14]. Alternately, Wróbel et al. [34] built a network out of cross-linked discrete viscoelastic elements and the corresponding elastic forces are computed on the Lagrangian coordinate system moving with the network. Similarly, we have developed a method for viscoelastic materials in which stress relaxation is imposed on a Lagrangian frame, but unlike the work in [34] we use a continuum-like approach. Rather than an expression for the time-evolution of the stress tensor, viscoelasticity is satisfied through a simple ordinary differential equation for how the reference

configuration of the material relaxes over time to the current configuration, which is derived from a continuum expression for how strain relaxes in times. We perform two rheological tests to reveal the mechanical response of such a material and show that in the limit of small strain, our formulation agrees with the linearised Maxwell model. Finally, the method is applied to cell locomotion through a microfluidic channel, where we demonstrate that the properties of the cytoplasm are important to capture the relevant biological behaviour.

2 Mathematical framework

2.1 Formulation of poroelasticity

To describe the mechanics of porous viscoelastic materials, we start with the two-phase flow model, which is often used to describe multicomponent mixtures that consist of an elastic network immersed in an incompressible, viscous fluid [5]. Because the aim of this work is to simulate the cytoskeleton, and the volume fraction of the cytoskeletal network is small in comparison to the fluid phase [18], we consider the case of negligible volume fraction of the elastic network. It was shown in Strychalski et al. [30] that the formulation used here matches the standard model of poroelastic media given by Biot [2] in the limit of vanishing network volume fraction. Here, we revisit the poroelasticity immersed boundary framework, and consider how to introduce stress relaxation within this method in order to capture the viscous behaviour of the cytoskeleton on longer timescale due to the reorganisation of the actin filaments.

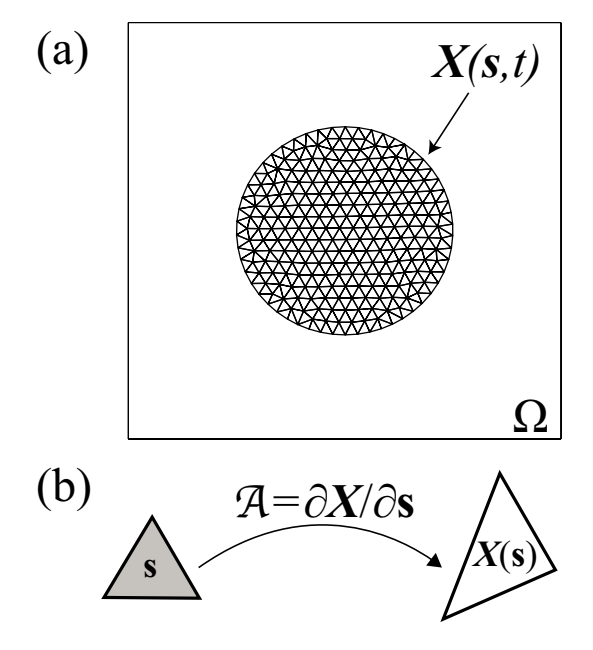


Figure 1: Computational domain and its discretisation. (a) Ω indicates the Eulerian domain with coordinate x. X(s,t) represents the current location of the Lagrangian variables with coordinate s. An unstructured grid is used to discretised the Lagrangian domain. The fluid variables are evaluated at the material points, x = X(s,t). (b) The deformation gradient tensor \mathcal{A} maps the vertices of the undeformed (reference) triangle configuration, s, to the deformed triangle configuration, x.

We consider a viscous incompressible fluid in a domain Ω containing an immersed structure, Γ . A natural way of representing the time evolution of a deforming elastic structure is with a moving Lagrangian coordinate system. The configuration of the structure is denoted by X(s,t), where s is a reference Lagrangian coordinate (Fig. 1a). We use the convention that capitalised letters represent material variables and lower case letters indicate fluid variables. We evaluate the fluid variables at the material points x = X(s,t) that define the spatial configuration of the material. In our formulation, there are separate force balance equations for the viscous fluid and for the internal elastic stresses on the structure. Each structure moves with its own velocity field and the two materials are coupled through drag forces. The force balance on the fluid includes internal fluid forces (viscosity, pressure) and drag force due to the relative motion of the immersed structure, which leads to the forced incompressible Stokes equations:

$$\mu \Delta \boldsymbol{u} - \nabla p + \boldsymbol{f}_{\text{drag}} = 0 \tag{1}$$

$$\nabla \cdot \boldsymbol{u} = 0, \tag{2}$$

where u represents the fluid velocity, p is the pressure, μ is the dynamic viscosity of the fluid. f_{drag} represents the drag force density on the fluid due to the relative motion of the structure and it is given by

$$\mathbf{f}_{\text{drag}} = \xi(\mathbf{U} - \mathbf{u}) , \qquad (3)$$

where U denotes the material velocity. The force density balance on the immersed structure is

$$F_{\text{drag}} + F_{\text{elastic}} = 0, \qquad (4)$$

where F_{elastic} denotes the elastic force density in the structure, and the drag force density on the structure is equal and opposite to the drag force density on the fluid,

$$F_{\text{drag}}(s,t) = -f_{\text{drag}}(x,t). \tag{5}$$

where the fluid variables are evaluated at the material points x = X(s, t). Combining Eqs. 3-5 and isolating the variable for the velocity of the structure, the structure moves as follows,

$$\frac{\partial \mathbf{X}}{\partial t} = \mathbf{U} = \frac{1}{\xi} \mathbf{F}_{\text{elastic}} + \mathbf{u} . \tag{6}$$

Given a set of elastic forces, the evolution of the elastic network specified in Eq. 6 in conjunction with the viscous flow equations in Eqs. 1-2 are sufficient to determine the dynamics of the fluid-structure system.

At this point, a constitutive law must be specified to compute the elastic forces of the material in Eq. 6. A general framework for describing elastic structures is by directly computing the force from energy functionals and without the direct use of stress tensors. Here, we consider hyperelastic materials, which are characterised by a strain energy density $W = W(\mathcal{A})$ where $\mathcal{A} = \partial X/\partial s$ is the network deformation gradient tensor [20]. For such materials, the Lagrangian elastic force density is given by the variational derivative of the energy:

$$F_{\text{elastic}} = -\frac{\delta E}{\delta X}$$
, (7)

where E is the total energy of the system,

$$E = \int_{\Gamma} W(\mathcal{A}) \, d\mathbf{s} \,. \tag{8}$$

The material properties of the hyperelastic solid are specified by a constitutive law for the strain energy density. For example, the strain energy density of a two-dimensional (2D) neo-Hookean elastic material is

$$W(\mathcal{A}) = \frac{G}{2} \left(\frac{\operatorname{tr}(\mathcal{A}\mathcal{A}^T)}{J^2} - 2 \right) + \frac{K}{2} (J - 1)^2 , \qquad (9)$$

where G denotes the elastic shear modulus, K is the elastic bulk modulus, and $J = \det A$ is the determinant of the deformation gradient tensor [20].

2.1.1 Discretisation of the model

Given the reference configuration of a material, the structure is discretised into a triangular mesh. Further, we assume that the deformation map $\boldsymbol{X}(s,t)$ is piecewise linear on each triangle T. For a given triangular element T, the positions of the k-th vertex of T in reference configuration are denoted by $\boldsymbol{s}^{(k)}$ whereas in the deformed configuration they are $\boldsymbol{X}^{(k)}$. The set of vectors that describe the deformed and undeformed triangular elastic sheets are $\widetilde{\boldsymbol{X}}^{(i)} = \boldsymbol{X}^{(i)} - \boldsymbol{X}^{(0)}$ and respectively, $\widetilde{\boldsymbol{s}}^{(i)} = \boldsymbol{s}^{(i)} - \boldsymbol{s}^{(0)}$ for i = 1, 2. Since a linear deformation was assumed on a triangle, the deformed triangular element is given by the following mapping,

$$\left(\widetilde{\boldsymbol{X}}^{(1)}\ \widetilde{\boldsymbol{X}}^{(2)}\right) = \mathcal{A}\left(\widetilde{\boldsymbol{s}}^{(1)}\ \widetilde{\boldsymbol{s}}^{(2)}\right),\tag{10}$$

where A is the deformation gradient tensor (shown in Fig. 1b).

For a piecewise linear deformation map, the deformation gradient tensor and the strain energy density are constant on each triangle. Starting with Eq. 7 and following the derivation in [30] and [8], the n-th component of the force (not force density) at vertex k contributed by triangle T is given by

$$\left(\widehat{\boldsymbol{F}}_{T}^{(k)}\right)_{n} = -\sum_{i,j=1}^{2} \mathcal{P}_{ij} \frac{\partial \mathcal{A}_{ij}}{\partial X_{n}^{(k)}} dA_{0}(T). \tag{11}$$

Here,

$$\mathcal{P}_{ij} = \partial W / \partial \mathcal{A}_{ij} , \qquad (12)$$

denotes the first Piola-Kirchhoff stress tensor. The area of the triangular element in reference configuration is denoted by $dA_0(T)$. To find the total force at the k-th vertex, we sum over the set of all triangles in the triangular mesh that contain vertex k, \mathcal{T}_k . To calculate the force density at each vertex as needed in the structure force balance in Eq. 4, we divide the force in Eq. 11 by the characteristic area of a node, dA_k , which is taken to be the sum of one third the area of each triangle with vertex X_k :

$$\boldsymbol{F}_{\text{elastic}}^{(k)} = \frac{\sum_{T \in \mathcal{T}_k} \widehat{\boldsymbol{F}}_T^{(k)}}{dA_k} = \frac{\sum_{T \in \mathcal{T}_k} \widehat{\boldsymbol{F}}_T^{(k)}}{\frac{1}{3} \sum_{T \in \mathcal{T}_k} dA_0(T)}$$
(13)

Notably, the Lagrangian elastic force density depends on the first Piola-Kirchhoff stress tensor which is a measure of the forces in the deformed configuration acting on an element of area in the reference configuration. By choosing a constitutive law for $W(\mathcal{A})$ or equivalently, \mathcal{P} , the type of material is specified.

2.2 Formulation for viscoelasticity

To simulate immersed elastic materials that exhibit rearrangement of the network, such as the cell cytoskeleton, we extend the existing framework for simulating poroelastic material [30] to capture stress relaxation in a moving Lagrangian coordinate system. Specifically, the aim is to introduce viscoelasticity congruent with the method for computing elastic forces outlined in Section 2.1.

For simplicity, we first consider a 2D incompressible neo-Hookean material. Then, the constitutive law in Eq. 9 reduces to the following expression [17, 20],

$$\sigma = GC, \tag{14}$$

where σ is the Cauchy stress tensor and C is the Finger deformation tensor which describes the change in shape of a small material element:

$$C = \mathcal{A}\mathcal{A}^T. \tag{15}$$

Alternatively, one can show that the constitutive law for an incompressible neo-Hookean material can be written as,

$$\begin{cases} \sigma = GC \\ \overset{\nabla}{C} = \frac{\partial C}{\partial t} + \boldsymbol{U} \cdot \nabla C - \nabla \boldsymbol{U} \cdot C - C \cdot \nabla \boldsymbol{U}^T = 0 \end{cases}, \tag{16}$$

where $\overset{\triangledown}{C}$ is called the upper-convected derivative [17, 20]. Here, the Finger tensor is a measure of the strain. Now, we introduce the relaxation of the strain to the identity matrix with a relaxation timescale, λ_T :

$$\lambda_T \stackrel{\triangledown}{C} = I - C \,, \tag{17}$$

Together, Eqs. 14 and 17 can also be written as a relaxation of the Cauchy stress tensor:

$$\lambda_T \stackrel{\triangledown}{\sigma} + \sigma = GI. \tag{18}$$

This expression is commonly identified as the upper-convected Maxwell model and it is one of the simplest non-linear models for stress relaxation which is analogous to the Maxwell element, a spring and dashpot in series [17, 20].

This formulation of viscoelasticity poses a few implementation difficulties for our immersed poroelastic framework. First, while elastic forces are computed in a moving, deforming frame in Section 2.1, the upper-convected Maxwell model would require computing a corresponding Cauchy stress tensor, and updating the Cauchy stress tensor in an Eulerian reference frame. One way to resolve this issue would be a change of coordinate system every time step [11, 14]. Furthermore, for the case of deforming and moving structures as is the case in cell locomotion, solving the partial differential equation in Eq. 18 throughout the structure every time step poses computational difficulties. To avoid both of these complications, we propose a simple model for viscoelasticity in a moving frame which is analogous to the upper-convected Maxwell model in Eqs. 14-17 (or equivalently, Eq. 18). In particular, we exploit the fact that our elasticity formulation in Eq. 11 involves the first Piola-Kirchhoff stress tensor and develop a model for viscoelasticity expressed for the first Piola-Kirchhoff stress tensor. This is achieved by following the same derivation as outline above to arrive at the upper-convected Maxwell model.

The first Piola-Kirchhoff tensor and the Cauchy stress tensor are related by

$$\mathcal{P} = J\sigma \mathcal{A}^{-T},\tag{19}$$

which relates quantities defined in areas in a deformed configuration to those relative to areas in a reference configuration [17, 20]. We express the Cauchy stress in the above relation in terms of the deformation gradient using Eqs. 14 and 15, and use that for an incompressible material $J = \det(A) = 1$ to express the constitutive law for an incompressible neo-Hookean material as

$$\mathcal{P} = G\mathcal{A} . \tag{20}$$

For an elastic material, the deformation gradient satisfies

$$\overset{\triangledown}{\mathcal{A}} = \frac{\partial \mathcal{A}}{\partial t} + \boldsymbol{U} \cdot \nabla \mathcal{A} - \nabla \boldsymbol{U} \cdot \mathcal{A} = 0. \tag{21}$$

Equations 20 and 21 are equivalent to 16. We note that the form of the upper-convected derivative of the deformation gradient, A, is slightly different than that of the Finger tensor, C, [17]. One can realise their equivalence by applying the derivative defined in Eq. 21 to $C = AA^T$.

The upper-convected Maxwell model results from introducing strain relaxation in a neo-Hookean material (i.e. as in Eq. 17). Analogously, we modify the elastic model from Eqs. 20–21 to describe a viscoelastic material by assuming that the deformation relaxes as

$$\lambda_T \stackrel{\triangledown}{\mathcal{A}} = I - \mathcal{A} \ . \tag{22}$$

Although Eq. 22 is chosen to be analogous to Eq. 17, in general, this will not produce the same material response as the upper-convected Maxwell model. In Section 3, we will provide both analytical and numerical comparisons of this model with the Maxwell model for two different rheological tests.

2.2.1 Discretisation of the model

Just as before, the structure is discretised into a triangular mesh with the assumption that deformation map is a linear on each triangle T and thus, the deformation gradient tensor is constant on each triangular element. However, instead of solving Eq. 22 on every triangular element, we propose an even simpler formulation of viscoelasticity by deriving a mathematically equivalent relation for how the material's reference configuration, s, relaxes to the current configuration, X, over time,

$$A\frac{\partial \mathbf{s}}{\partial t} = \frac{1}{\lambda_T} (\mathbf{X} - \mathbf{s}). \tag{23}$$

We claim that the above expression is equivalent to the relaxation of the strain in Eq. 22 provided that A is constant per triangular element. To show this, we start with the definition of the deformation gradient tensor,

$$A = \frac{\partial X}{\partial s},\tag{24}$$

where now because the reference configuration evolves in time, it is useful to express the current and reference configuration variables as functions of time and the particle label, α . Then, by the chain rule,

$$\mathcal{A}_{ij} = \frac{\partial \mathbf{X}_i}{\partial \boldsymbol{\alpha}_k} \frac{\partial \boldsymbol{\alpha}_k}{\partial \mathbf{s}_j},\tag{25}$$

where $\boldsymbol{X} = \boldsymbol{X}(t, \boldsymbol{\alpha})$ and similarly, $\boldsymbol{s} = \boldsymbol{s}(t, \boldsymbol{\alpha})$. A rearrangement of the above equation yields,

$$A\frac{\partial s}{\partial \alpha} = \frac{\partial X}{\partial \alpha}.$$
 (26)

which can now be differentiated in time to obtain

$$\frac{\partial \mathcal{A}}{\partial t} \frac{\partial \mathbf{s}}{\partial \boldsymbol{\alpha}} + \mathcal{A} \frac{\partial}{\partial \boldsymbol{\alpha}} \left(\frac{\partial \mathbf{s}}{\partial t} \right) = \frac{\partial \mathbf{U}}{\partial \boldsymbol{\alpha}} , \qquad (27)$$

where $U = \partial X/\partial t$. At this point, for the partial time derivative of s we assume that the reference configuration relaxes as in Eq. 23, and obtain the following equation,

$$\frac{\partial \mathcal{A}}{\partial t} \frac{\partial \mathbf{s}}{\partial \boldsymbol{\alpha}} - \frac{\partial \mathbf{U}}{\partial \boldsymbol{\alpha}} = -\mathcal{A} \frac{\partial}{\partial \boldsymbol{\alpha}} \left(\frac{\partial \mathbf{s}}{\partial t} \right) = -\frac{1}{\lambda_T} \mathcal{A} \frac{\partial}{\partial \boldsymbol{\alpha}} \left(\mathcal{A}^{-1} (\mathbf{X} - \mathbf{s}) \right) = -\frac{1}{\lambda_T} \frac{\partial}{\partial \boldsymbol{\alpha}} \left(\mathbf{X} - \mathbf{s} \right), \quad (28)$$

which holds under the assumption that the deformation gradient tensor is constant per triangle. In the above equations, all quantities are expressed as functions of α . To change coordinates and express quantities as functions of s, we use that

$$\frac{\partial}{\partial \alpha_i} = \frac{\partial s_j}{\partial \alpha_i} \frac{\partial}{\partial s_j} \tag{29}$$

to obtain

$$\frac{D\mathcal{A}}{Dt} - \frac{\partial \mathbf{U}}{\partial \mathbf{s}} = -\frac{1}{\lambda_T} \frac{\partial}{\partial \mathbf{s}} \left(\mathbf{X} - \mathbf{s} \right) = -\frac{1}{\lambda_T} \left(\frac{\partial \mathbf{X}}{\partial \mathbf{s}} - I \right) = \frac{1}{\lambda_T} \left(I - \mathcal{A} \right), \tag{30}$$

where $D\mathcal{A}/Dt = \partial \mathcal{A}/\partial t + \mathbf{U} \cdot \nabla_s \mathcal{A}$ is the material derivative. Lastly, a transformation to the Eulerian coordinate system yields,

$$\frac{D\mathcal{A}}{Dt} - \frac{\partial \mathbf{U}}{\partial \mathbf{X}} \mathcal{A} = \frac{1}{\lambda_T} \left(I - \mathcal{A} \right), \tag{31}$$

using the following change of coordinates,

$$\frac{\partial \boldsymbol{U}}{\partial \boldsymbol{s}} = \frac{\partial \boldsymbol{U}}{\partial \boldsymbol{X}} \frac{\partial \boldsymbol{X}}{\partial \boldsymbol{s}} = \frac{\partial \boldsymbol{U}}{\partial \boldsymbol{X}} \boldsymbol{\mathcal{A}},$$

where now, $D\mathcal{A}/Dt = \partial \mathcal{A}/\partial t + \mathbf{U} \cdot \nabla \mathcal{A}$. Indeed, we find that the expression for the convective derivative of the deformation gradient tensor in Eq. 22 is recovered in Eq. 31.

In this framework, we model the stress relaxation of a material through only the ordinary differential equation for the reference configuration and the stress-strain relation is given by specifying a constitutive law for the first Piola-Kirchhoff stress tensor. This rearrangement has the advantage that viscoelasticity is imposed in a computationally inexpensive way and does not depend on the constitutive law or the mesh discretisation of the material. Thus, the equations of motion for the immersed porous viscoelastic structure and the incompressible viscous fluid are:

$$\mu \Delta \boldsymbol{u} - \nabla p + \boldsymbol{f}_{\text{drag}} = 0 \tag{32}$$

$$\nabla \cdot \boldsymbol{u} = 0 \tag{33}$$

$$\mathbf{F}_{\text{elastic}} + \mathbf{F}_{\text{drag}} = 0$$
 (34)

$$\mathcal{A}\frac{\partial \boldsymbol{s}}{\partial t} = \frac{1}{\lambda_T}(\boldsymbol{X} - \boldsymbol{s}), \qquad (35)$$

where the drag force density on the fluid due to the network is:

$$\mathbf{f}_{\text{drag}} = -\mathbf{F}_{\text{drag}} = \xi(\mathbf{U} - \mathbf{u}) . \tag{36}$$

The elastic force density on the structure, $F_{\rm elastic}$, is computed through a variational derivative of the energy as described in Eqs. 11-13. Combining Eqs. 34 and 36, we find that the drag force density on the fluid is equal to the elastic force density on the structure, $f_{\rm drag} = -F_{\rm drag} = F_{\rm elastic}$ and replacing in Eq. 32 yields

$$\mu \Delta \boldsymbol{u} - \nabla p + \boldsymbol{F}_{\text{elastic}} = 0. \tag{37}$$

Given the configuration of the material, Eqs. 37 and 33 determine the fluid velocity and pressure, and Eq. 6 determines the structure velocity. The structure's position and rest configuration evolve in time according to Eq. 6 and Eq. 35, respectively.

3 Rheological validations

In this section, we validate the framework for simulating porous, viscoelastic materials permeated by viscous fluid by comparing with continuum equations for a viscoelastic structure. Specifically, we carry out rheological measurements of a material with a viscoelastic response in the limit of small deformations in order to compare with analytical expressions for the stress tensor. Here, we present two rheological tests used to characterise viscoelastic properties: a small amplitude oscillatory shear test and a dynamic expansion test. In the small amplitude oscillatory shear test, a periodic deformation is imposed on the material and the resulting deformation gradient tensor and stress are measured. In the expansion test, the material is stretched uniformly in the radial direction and the velocity profile throughout time and space is obtained and compared with the linearised Maxwell model in the limit of small strain.

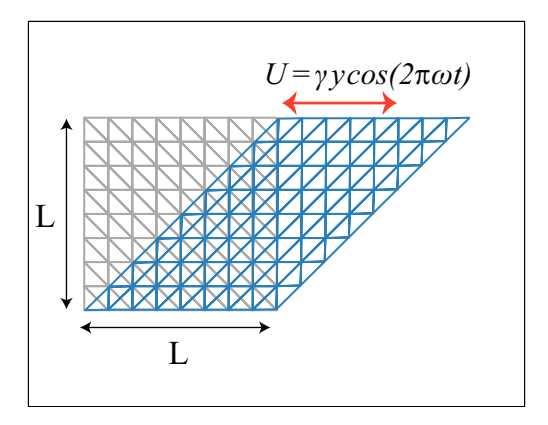


Figure 2: Schematic for oscillatory linear shear test. A square viscoelastic material undergoes a prescribed oscillatory motion in the horizontal direction as given by Eq. 39 with amplitude γ and frequency ω . The initial material configuration is shown in grey while the later in time configuration is in blue. We note that the deformation is not drawn to scale.

3.1 Small amplitude oscillatory shear test

We consider a test problem with a prescribed deformation through time and we measured the strain response of the material. For this problem, a periodic linear shear is imposed on a square viscoelastic

structure with side of length L (Fig. 2). The prescribed network velocity is

$$\boldsymbol{U} = (U(y), 0) = (\gamma y \cos(2\pi\omega t), 0), \qquad (38)$$

Since the current position and velocity are related by $\partial X/\partial t = U$, the position of the structure at a given time is

$$X = (\gamma y \sin(2\pi\omega t)/(2\pi\omega), 0). \tag{39}$$

In this section, we will use this rheological test to provide two insights about the framework described in Section 2.2: first, a numerical validation that the differential equation for the reference configuration in Eq. 35, is indeed equivalent to the relaxation of the deformation gradient tensor in Eq. 22, and secondly, a comparison of our model for viscoelasticity and the linearised Maxwell model in the limit of small deformation (or strain).

3.1.1 Numerical validation

First, to validate the stress relaxation response of the poro-viscoelastic formulation, we compare the deformation gradient tensor that is obtained by solving Eq. 22, to a 2D prescribed motion simulation, where stress relaxation is imposed by the simple update expression for the reference configuration in Eq. 35. For the oscillatory linear shear motion in Eq. 38, with the convention that the gradient of the vector is $\nabla U = \partial U_i/\partial X_j$, the gradient of the velocity of the structure is

$$\nabla \boldsymbol{U} = \begin{pmatrix} 0 & \gamma \cos(2\pi\omega t) \\ 0 & 0 \end{pmatrix}. \tag{40}$$

We note that the gradient of the structure velocity is constant in space for this prescribed motion test. Then, the time-evolution for strain in Eq. 22 is written component-wise as,

$$\lambda_T \left(\frac{\mathcal{A}_{11}}{\partial t} - \gamma \cos(2\pi\omega t) \mathcal{A}_{21} \right) + \mathcal{A}_{11} = 1, \tag{41}$$

$$\lambda_T \left(\frac{\mathcal{A}_{12}}{\partial t} - \gamma \cos(2\pi\omega t) \mathcal{A}_{22} \right) + \mathcal{A}_{12} = 0, \tag{42}$$

$$\lambda_T \frac{\mathcal{A}_{21}}{\partial t} + \mathcal{A}_{21} = 0, \tag{43}$$

$$\lambda_T \frac{\mathcal{A}_{22}}{\partial t} + \mathcal{A}_{22} = 1. \tag{44}$$

Initially, because there is no deformation of the material, the deformation gradient tensor is $\mathcal{A}(0) = I$. With this initial condition, the full analytical solution to the components of the deformation gradient tensor are

$$\mathcal{A}_{11}(t) = 1, \tag{45}$$

$$\mathcal{A}_{12}(t) = \frac{\gamma \lambda_T}{4\pi^2 \omega^2 \lambda_T^2 + 1} \left(-e^{-t/\lambda_T} + \cos(2\pi\omega t) \right) + \frac{2\pi\omega\gamma\lambda_T^2 \sin(2\pi\omega t)}{4\pi^2 \omega^2 \lambda_T^2 + 1}, \tag{46}$$

$$\mathcal{A}_{21}(t) = 0, \tag{47}$$

$$A_{22}(t) = 1.$$
 (48)

For this test, we set $\xi=0.1$, $\lambda_T=0.5$, G=0.5, L=1.0, and $t\in[0,5]$ in arbitrary units. For the prescribed motion in Eq. 38, we set $\gamma=0.5$ and $\omega=1.0$. In this scenario, the motion of

the structure is prescribed, and the reference configuration of the material is obtained using Eq. 35 updated with the forward-Euler method for time integration. Because only the 12-component of the deformation gradient tensor is non-constant, the convergence of only this component is discussed here. Fig. 3a shows the difference between the analytically computed deformation gradient and the resulting deformation gradient from the simulation normalised by maximum deformation gradient tensor over time. Since for this test problem ∇U is constant in space, there is no spatial error for this rheological test. Here, the temporal discretisation chosen is $\Delta t = 10^{-7}$ in arbitrary time units. In Fig. 3b we show the error at t = 2.2 (chosen near one of the peaks in Fig. 3a) for different time steps. The model shows a first-order convergence in time when compared to the line of slope 1 in the plot.

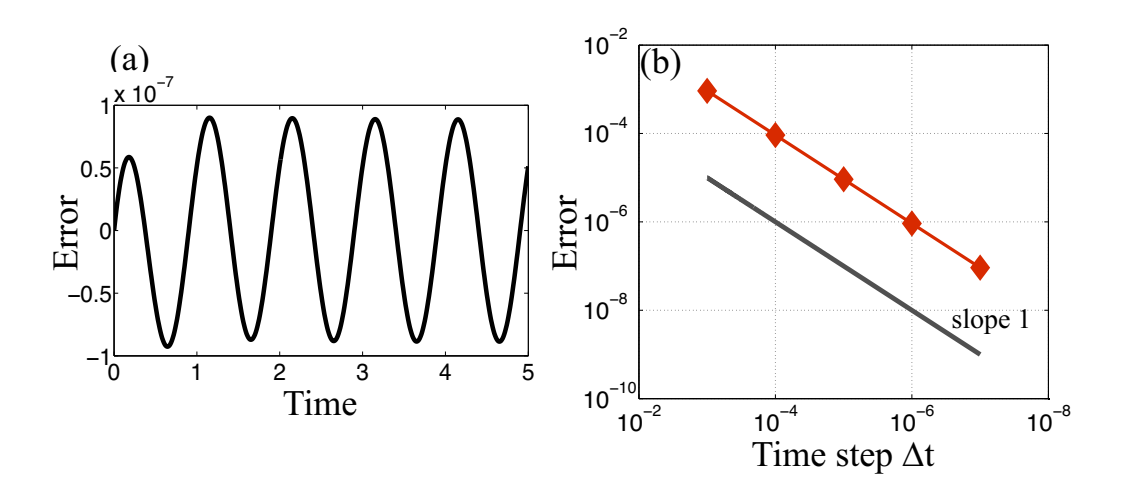


Figure 3: Relative error in the deformation gradient tensor for an oscillatory linear shear test. (A) Shown here is a plot of the difference between the analytically computed deformation gradient tensor and the resulting deformation gradient tensor normalised by its maximum over time for an oscillatory linear shear test. (B) The difference between the analytical solution of the deformation gradient tensor and the deformation gradient tensor obtained from the 2D prescribed motion simulation is scaled by its maximum at t=2.2 and plotted for different choices of time step.

3.1.2 Comparison with linear viscoelasticity

Next, the same deformation of an oscillatory linear shear is considered, but in the limit of small amplitude deformations, $\gamma \ll 1$. To demonstrate that our method agrees with known models for linear viscoelasticity, we compare the Cauchy stress tensor obtained by solving the linearised Maxwell model in Eq. 18 to a 2D prescribed motion simulation as in Eqs. 32-35. This comparison is presented analytically below and also numerically in Fig. 4.

In the 2D prescribed motion simulation, the Cauchy stress tensor is given by the stress-strain relation, $\sigma = G\mathcal{A}\mathcal{A}^T$. Using the analytical form of the deformation gradient tensor for oscillatory shear derived in Eqs. 45-48, we arrive at the following full expression for the Cauchy stress tensor in the porous, viscoelastic method proposed in this work:

$$\sigma(t) = \begin{pmatrix} G + G\mathcal{A}_{12}^2 & G\mathcal{A}_{12} \\ G\mathcal{A}_{12} & G \end{pmatrix} , \tag{49}$$

where the functional form of $A_{12} = A_{12}(t)$ is provided in Eq. 46. In particular, in the limit of infinitesimal strain, the quadratic term in the 11-component of the Cauchy stress tensor is negligible. To find the solution to the linearised Maxwell model in Eq. 18 in the limit of small strain, first we linearise the expression about the equilibrium, $\sigma = \tau + GI$, to arrive at the following expression,

$$\lambda_T \frac{\partial \tau}{\partial t} + \tau = 2\lambda_T GD , \qquad (50)$$

where $D = 1/2(\nabla U + \nabla U^T)$ is the rate-of-deformation tensor. With the deformation in Eq. 38, the solution is given by,

$$\tau = \begin{pmatrix} 0 & \tau_{12} \\ \tau_{12} & 0 \end{pmatrix} ,$$

where τ_{12} satisfies the equation,

$$\lambda_T \left(\frac{\partial \tau_{12}}{\partial t} - G\gamma \cos(2\pi\omega t) \right) + \tau_{12} = 0.$$
 (51)

We note that this equation is identical to the equation for A_{12} in Eq. 42 since $A_{22}(t) = 1$ and provided that $\tau_{12} = GA_{12}$. Therefore, the Cauchy stress tensor for the linearised Maxwell model in the case of small amplitude oscillatory shear has the form:

$$\sigma = \begin{pmatrix} G & G\mathcal{A}_{12} \\ G\mathcal{A}_{12} & G \end{pmatrix} + O(\gamma^2) , \qquad (52)$$

since $A_{12}(t) \propto \gamma$. Up to quadratic terms in the amplitude of the oscillation, Eqs. 52 and 49 match; our method for stress relaxation is in good agreement with the linearised Maxwell model in the limit of small strain.

Next, we also provide numerical validation for this agreement. Using the same parameters as in the previous section but with $\gamma=10^{-3}$, the relative difference in each component of the Cauchy stress tensor between the full 2D prescribed motion simulation and the linearised equation for the Maxwell material are shown in Fig. 4. We observe that the relative difference in the first component of the Cauchy stress tensor is slightly lower that the magnitude of the amplitude squared, $O(10^{-8}) < O(\gamma^2)$, which is in good agreement with our claim that the methods match up to quadratic terms in strain.

3.2 Linear expansion test

Since the deformation was prescribed in the previous rheological test, we now consider a dynamical test in which a radially symmetric material is expanded uniformly. The motion of the boundary of a circular viscoelastic structure of radius R is prescribed to move in the outward normal direction with velocity as shown in Fig. 5. In this case, the fluid velocity is zero, and the motion of the interior of the material is found by solving the system in Eqs. 32-34,

$$\nabla \cdot \sigma - \xi \mathbf{U} = 0. \tag{53}$$

For tractability of an analytical solution, we consider a simple model of a compressible material,

$$\sigma = G\mathcal{A}\mathcal{A}^T \,, \tag{54}$$

where now, G denotes an elastic modulus. We will use this rheological test to evaluate the material response over time due to a perturbation at the boundary and compare the response with the linearised Maxwell model.

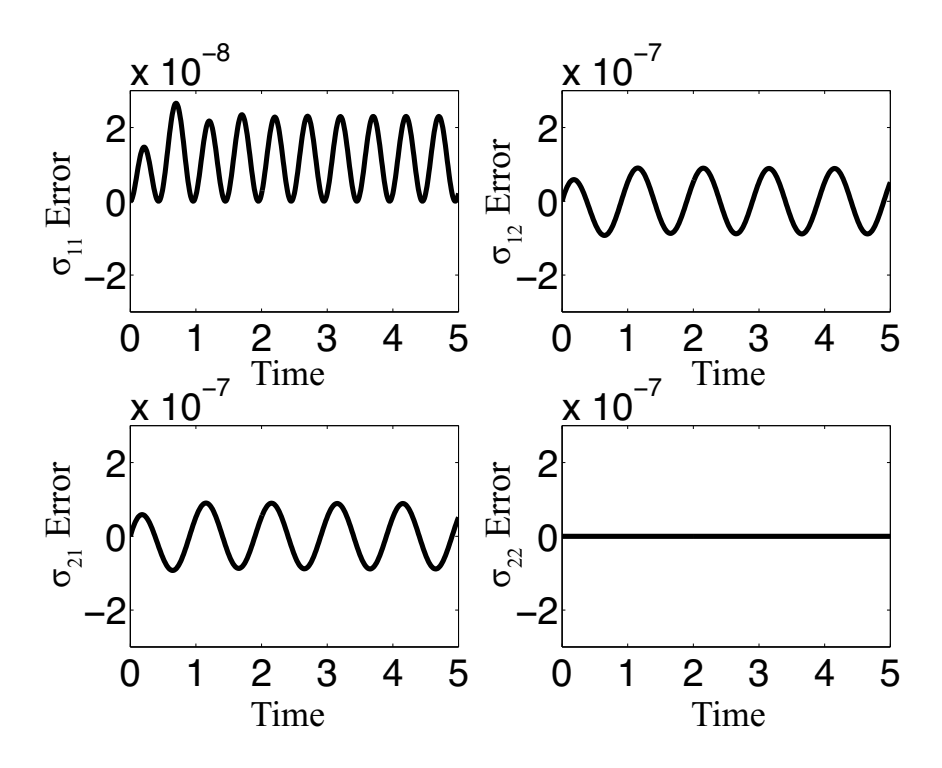


Figure 4: Comparison of a full 2D prescribed motion simulation with linear viscoelasticity for a small amplitude oscillatory shear test. Shown here are the relative differences in the stress components between the analytically computed stress for linearised Maxwell model and the computed stress in the prescribed motion simulation; both stress measurements are normalised by the maximum stress over time.

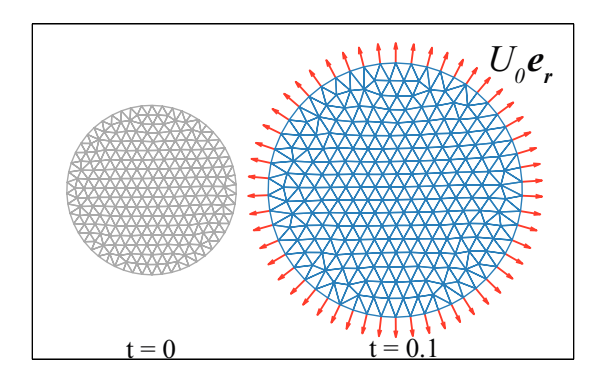


Figure 5: Schematic for linear expansion test. A viscoelastic unit circular material undergoes an expansion in the radial direction driven by a prescribed motion at the boundary. The initial material configuration is shown in grey while the later configuration at time t=0.1 is in blue. The arrows indicate the velocity at the boundary that drives the expansion of the material. We note that the deformation is not drawn to scale; in our simulations the relative deformation is 10^{-3} .

3.2.1 Numerical validation

We compare the velocity U(r,t) that is obtained from a full 2D immersed structure simulation where viscoelasticity is modelled by the simple differential equation in Eq. 35, to an analytical solution of

the linearised Maxwell model (as in Eq. 18). Specifically, we linearise the upper-convected Maxwell model and the force balance in Eq. 53 and find a series solution to the radial velocity, $U(r,t) = (U_r, U_\theta) = (U_r, 0)$, in Appendix A. Here, $U_r = U \cdot e_r$ and $U_\theta = U \cdot e_\theta = 0$ correspond to the radial and angular components of the velocity. Since in this test problem, the material experiences a prescribed velocity in the radial direction on the boundary, we take the following boundary condition,

$$U_r(R,t) = U_0 (55)$$

for some velocity U_0 . We also assume that initially, the network undergoes no deformation: $U_r(r,0)=0$. For this section, we set $\xi=0.5$, $\lambda_T=0.05$, G=1.0, R=1.0, and $t\in[0,0.1]$ in arbitrary units. The radial velocity at the boundary is set to be $U_0=10^{-2}$, which corresponds to a uniform expansion of the disk 0.1% in the radial direction. The series solution is truncated after 10 terms with a truncation error less than $\mathcal{O}(10^{-16})$. For a poroelastic material, non-dimensionalisation can be used to show that stress propagates effectively diffusively through the material with a characteristic timescale of $R^2\xi/G$ [22, 31]. For these parameters, the poroelasticity diffusion timescale for propagation of the deformation is approximately 0.5 arbitrary time units, while the stress relaxation timescale is 0.05 arbitrary time units. The radial velocity through the material at several time points is shown in Fig. 6a. We observe that the material exhibits a fast equilibration within two relaxation time units.

For the numerical simulations, the Lagrangian domain is a unit disk that is discretised using Distmesh [25] with a uniform mesh size. The algorithm was used to generate an unstructured grid with 256 Lagrangian points with an averaged spatial discretisation of $\Delta s \approx 0.118686$. Internal elastic forces are computed based on the material's configuration. Specifically, for the computation of elastic force densities, we use the following constitutive law for the material, $\mathcal{P} = JG\mathcal{A}$, which is equivalent to the constitutive law for the Cauchy stress tensor in Eq. 54. The fluid velocity is zero because of incompressibility, and the material's position and reference configuration are updated in time using the forward-Euler method to integrate Eq. 6 and 35, respectively, with time step $\Delta t = 10^{-5}$.

In order to compare the numerical solution of the immersed structure simulation to the truncated series solution of Eqs. 18 and 53, we evaluate the series solution at the points on the Lagrangian grid. Convergence data is presented in Fig. 6b which shows L_{∞} and L_2 norms of the difference between the truncated series velocity in the radial direction and the velocity resulting from the simulation at t=0.1 for different grid refinements. Similar to the previous test, the model also shows first order convergence in both norms when compared to the line of slope 1 in the plot.

3.2.2 The effect of the relaxation timescale

By varying the relaxation timescale in the system, the material response in this modelling framework can be dominated by either the elastic or viscous timescales as illustrated in Fig. 7. In both simulations all parameters are kept fixed and in particular the diffusion timescale for the material is 0.5 arbitrary time units. In the first simulation, the relaxation timescale is $\lambda_T = 0.05$, while in the second simulation the relaxation timescale is much longer, $\lambda_T = 2.0$. For a small relaxation timescale, the stress imposed by the deformation is gradually forgotten over time since the memory of the stress has a time constant of $\lambda_T = 0.05$ arbitrary time units. This implies that over this characteristic timescale, the strain due to the initial deformation decays on the timescale of the problem. In the case of a large relaxation timescale, we conjecture that the material response should be well-described by an elastic solid. In Fig. 7, we see that by 0.1 arbitrary time units, the velocity profile is nearly linear across the material, which indicates that the initial deformation has propagated across the material. This is because the memory of the deformation is kept for a much longer timescale than the time of the simulation since,

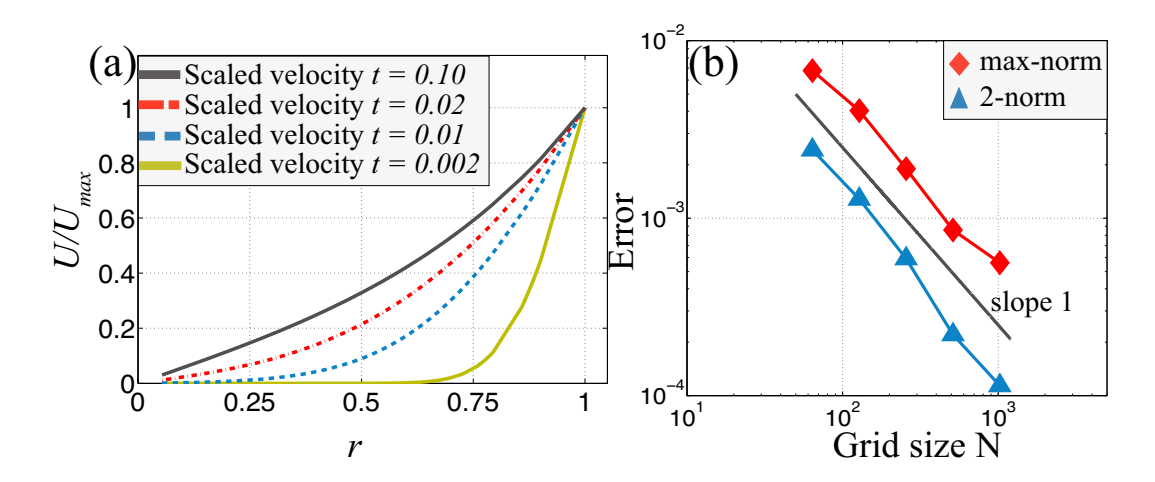


Figure 6: Relative error in the velocity profile of the immersed structure for a linear expansion test. (a) Given here is the velocity $U_r(r,t)$ in the radial direction at several time points divided by the maximum velocity $U_{\rm max}=1.0\times 10^{-2}$. (b) The 2-norm and max-norm of the difference between the truncated series solution of the velocity field and numerical solution scaled by the maximum velocity at t=0.1 is plotted for different grid sizes.

 λ_T is chosen to be 2.0 time units. A linear velocity profile is indeed what is expected in the case of elastic solid as seen by considering the limit $\lambda_T \to \infty$ of the steady state solution of the velocity profile in Appendix A. By varying the relaxation timescale, the rheological properties of the material can be tuned to be either more elastic or viscous.

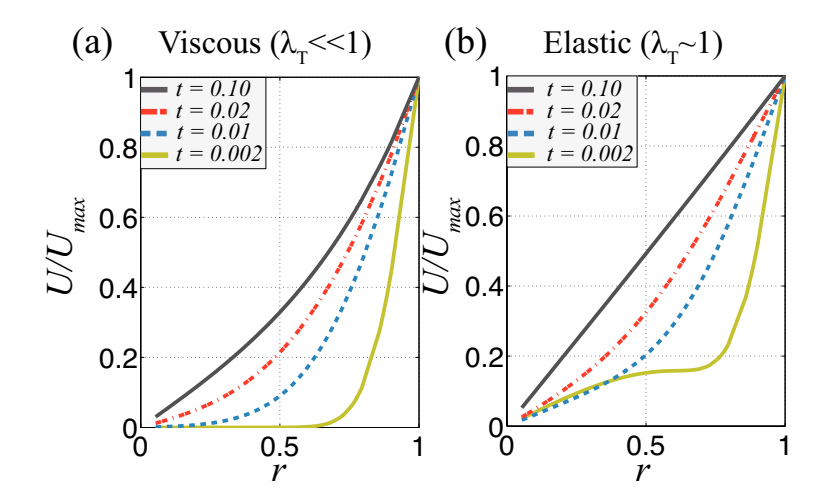


Figure 7: Velocity profiles across the radially symmetric material for different relaxation timescales. Shown here are different time plots of the scaled radial velocity $U_r(r,t)$ by the maximum velocity $U_{\rm max}=1.0\times 10^{-2}$. The time-space evolution of the scaled radial velocity is illustrated for the case of (a) small relaxation timescale, $\lambda_T=0.05$, and (b) relaxation timescale much longer than observable time, $\lambda_T=2$.

4 An application: Simulation of a cell in a microfluidic channel

In this section, the modelling framework for a porous, viscoelastic material immersed in viscous fluid is applied to simulate the cell cytoplasm as the cell is driven through a microfluidic channel due to a prescribed pressure difference on the extracellular fluid. Microfluidic devices have found numerous applications in biology, biochemistry, and medicine because of their ability to efficiently control and replicate microenvironments [32, 33]. Cell migration through microfluidic channels has gained interest as an experimental method for one-dimensional, directed migration and has been applied to study red blood cell flow in capillary-like microenvironments [28, 33], cell differentiation [4, 21, 29], and the role of interstitial flow in tumor cell migration [27].

In this section, the porous, viscoelastic framework described above is applied to study the effect of the cytoplasm rheology on the locomotion through a channel as illustrated in Fig. 8. Although microfluidic channels with chemical gradients have also been used to study directional chemotaxis [16], here we consider the passive locomotion of cells due to an extracellular fluid flow in the absence of chemotaxis and cell-surface adhesion. In this experimental setup, cells are driven through a confined environment in which rheology of the cytoplasm becomes an important factor in determining the escape time across this microenvironment. With this goal in mind, we compare two mechanical models of the cytoskeleton: poroelastic material and poro-viscoelastic material. Depending on the pressure gradient, the transient time is expected to be on the order of seconds to a few minutes and on this intermediate timescale, the rheological properties of the cytoskeleton have been measured [12] and are known to be well-described by a viscoelastic material [1, 13, 23]. Using this experimental setup, we demonstrate that the time for the cell to travel the length of the microfluidic channel is much longer with a poroelastic cytoskeleton than with a porous viscoelastic cytoskeleton where stress relaxation of the material has the effect of lowering the internal strain energy.

4.1 Model of the cell

Poroelastic cytoplasm model

The cell moves in the horizontal direction due to fluid flow from a prescribed pressure drop in a microfluidic channel as illustrated in Fig. 8. Our model of the cell has two subcellular components: a combined membrane-cortex structure and the cytoplasm. The cell cytoplasm is represented as a two-phase material: a viscous fluid phase (the cytosol) and a viscoelastic network (the cytoskeleton) with position X^{cyto} . The cell membrane and its underlying actomyosin cortex are represented as one structure and is modelled as an impermeable contractile elastic structure that moves with the fluid velocity. The position of the membrane/cortex structure is denoted by $X^{\text{mem}}(s,t)$, where s is the local parametric coordinate on the structure and $\hat{\tau}$ is the tangent vector to this curve. The membrane/cortex structure lies on the boundary of the cytoskeletal network and thus, in the discretisation of the method, the cytoskeleton and the membrane/cortex share discretisation points. This modeling choice is equivalent to requiring that the boundary of the cytoskeletal network and membrane/cortex structure are connected by rigid attachments on a lengthscale well below the mesh spacing. The force balance equation for the fluid phase includes the membrane/cortex structure, the cytoskeletal drag, as well as a repulsive interaction with the top and bottom channel walls,

$$\mu \Delta \boldsymbol{u} - \nabla p + \boldsymbol{f}_{\text{drag}}^{\text{cyto}} + \boldsymbol{f}_{\text{elastic}}^{\text{mem}} + \boldsymbol{f}_{\text{repulsive}}^{\text{mem}} = 0$$

$$\nabla \cdot \boldsymbol{u} = 0 ,$$
(56)

$$\nabla \cdot \boldsymbol{u} = 0, \tag{57}$$

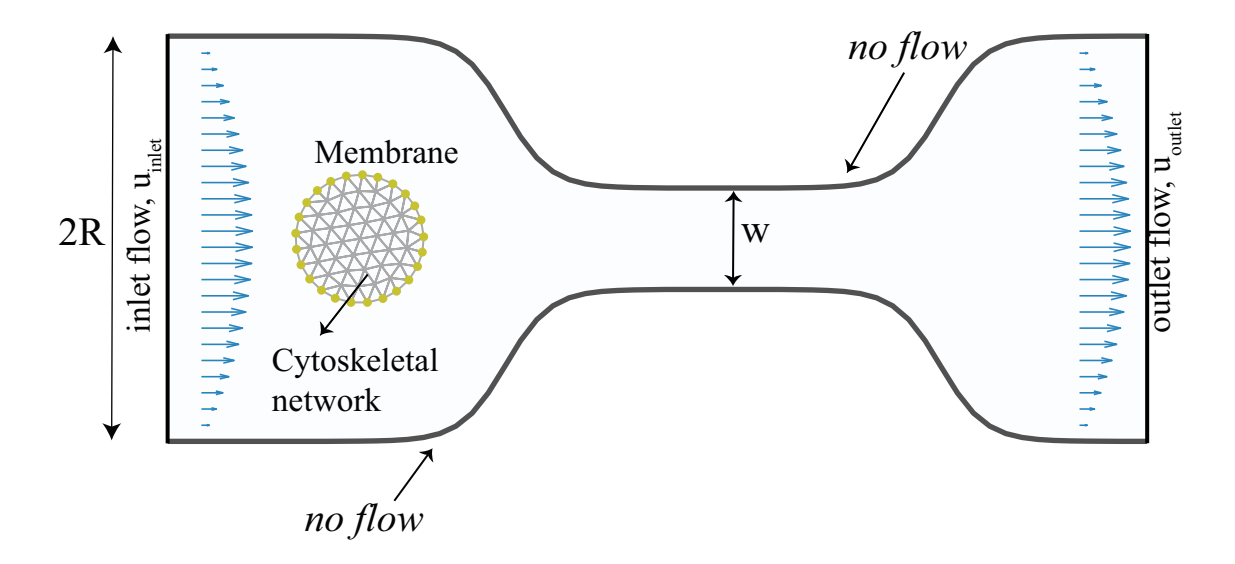


Figure 8: Schematic of the computational setup with a side view of a cell in a microfluidic channel. The fluid flow is driven by a prescribed pressure differential across the channel. The width of the channel in the narrowest section, w, is chosen to be 75% of the initial cell diameter. The arrows indicate the characteristic Poiseuille velocity field imposed at the endpoints of the channel. Our model of the cell has three subcellular components: a combined membrane-cortex structure, a viscous cytosol, and a cytoskeletal network.

where $f_{\text{drag}}^{\text{cyto}}$ is the drag force density on the fluid due to the relative motion of the structure. For the force densities, we use the convention that the subscript describes the type of force and the superscript describes the structure acted upon by the force. $f_{\text{elastic}}^{\text{mem}}$ is the elastic force density on the membrane/cortex structure and it is computed by

$$\mathbf{f}_{\text{elastic}}^{\text{mem}} = \frac{\partial}{\partial s} (T\hat{\tau}) .$$
 (58)

The tension T is given by

$$T = \gamma + k \left(\left| \frac{\partial \mathbf{X}^{\text{mem}}}{\partial s} \right| - 1 \right), \tag{59}$$

which describes a linearly elastic spring with stiffness k and resting tension γ . To capture non-specific, small lengthscale cell-surface interaction, when the cell membrane is within a distance δ_w of the channel wall, it experiences a repulsive force of the form

$$\mathbf{f}_{\text{repulsive}}^{\text{mem}} = \begin{cases} -k_{\text{repulsive}}(\delta_w - d)\,\widehat{n} , & d < \delta_w \\ 0 , & d \ge \delta_w . \end{cases}$$
(60)

Here, d denotes the distance from the top and bottom channel walls to the cell, $k_{\text{repulsive}}$ represents the stiffness of this repulsive interaction, and \widehat{n} is a unit vector in the outward normal direction. On the cytoskeletal network, the force density balance equation has the form,

$$F_{\text{drag}}^{\text{cyto}} + F_{\text{elastic}}^{\text{cyto}} = 0$$
 (61)

Here, the cytoskeletal drag is defined as $F_{\text{drag}}^{\text{cyto}} = -f_{\text{drag}}^{\text{cyto}} = \xi(u - U)$. The elasticity of the cytoskeletal network is computed as described in Section 2.1 with the strain energy density for a compressible, neo-Hookean material provided in Eq. 9.

Given a configuration of the membrane/cortex structure and the cytoskeleton, forces at every location on the structures are computed, and then the pressure and velocity of the fluid, along with velocity of the membrane/cortex and cytoskeleton are obtained by solving Eqs. 56-57 and Eq. 61. The positions of each structure are updated according to their own respective velocities,

$$\frac{d\boldsymbol{X}^{\text{mem}}}{dt} = \boldsymbol{u} \tag{62}$$

$$\frac{d\mathbf{X}}{dt} = \mathbf{u}$$

$$\frac{d\mathbf{X}^{\text{cyto}}}{dt} = \frac{1}{\xi} \mathbf{F}_{\text{elastic}}^{\text{cyto}} + \mathbf{u} .$$
(62)

Poro-viscoelastic cytoplasm model

The model formulation for a porous, viscoelastic cytoskeletal network is the same as above with the addition of stress relaxation of the material phase. Here, stress relaxation is imposed through the time-evolution equation for the reference configuration of the material as derived in Section 2.2. This implies that in addition to moving each structure according to their respective velocity fields as provided in Eqs. 62-63, the reference configuration of the each structure must also updated using Eq. 35.

4.2 Stokes fluid solver

The method of regularised Stokeslets is used to solve the Stokes fluid equations given the forces of the immersed structure. In order to drive the cell through the confined microenvironment, a pressure difference is imposed horizontally across the microfluidic channel while the top and bottom channel walls satisfy a no-slip boundary condition (Fig. 8). For the inlet and outlet flow, we prescribe a Poiseuille flow profile with an unknown maximum speed, u_{max} ,

$$\mathbf{u}_{\text{inlet/outlet}} = \left(u_{\text{max}}\left(1 - \frac{y^2}{R^2}\right), 0\right) = u_{\text{max}} \, \mathbf{v}_{\text{inlet/outlet}} \,,$$
 (64)

where R represents half the vertical separation between the channel walls. The other unknowns of this system are the forces at the vertical channel walls, $f_{\text{inlet/outlet}}$, which produce a parabolic flow profile, along with the forces along the top and bottom walls, f_{walls} , where the no-slip boundary condition is enforced. Then, algebraically, the system has the following form:

$$\begin{pmatrix} \mathcal{M} & \mathcal{C} \\ S \Pi & 0 \end{pmatrix} \begin{pmatrix} \mathbf{f} \\ u_{\text{max}} \end{pmatrix} = \begin{pmatrix} 0 \\ \Delta P \end{pmatrix} , \tag{65}$$

where

$$f = \begin{pmatrix} f_{\text{walls}} \\ f_{\text{inlet/outlet}} \end{pmatrix}, \quad C = \begin{pmatrix} 0 \\ -v_{\text{inlet/outlet}} \end{pmatrix}$$
 (66)

Here, \mathcal{M} denotes the regularised Stokeslet velocity matrix which maps regularised forces to flow velocities while Π represents the regularised Stokeslet pressure matrix which maps regularised forces to pressure. S is the discretisation of the operator which acts on a pressure field, p, as follows,

$$S p = \frac{1}{2R} \int_{-R}^{R} \left(p_{\text{outlet}} - p_{\text{inlet}} \right) dy.$$
 (67)

For a given channel geometry and pressure difference across the channel, ΔP , the system of equations is solved for the unknown forces and flow constant, u_{max} .

4.3 Discretisation of the model

To simulate the dynamics of a cell driven by an external pressure drop, the cytoskeletal network is spatially discretised using 62 points and every discrete point has its own current and reference position and velocity field. The averaged spatial discretisation is $\Delta s = 2.0\,\mu\text{m}$. The boundary points on the network form the membrane/cortex structure. Every time instance, local forces are computed at every discretised point along the cytoskeletal network and the membrane/cortex structure and their position is updated according to their respective update equations (Eqs. 62-63). A finite difference scheme is used to evaluate spatial derivatives in the force computations. Eqs. 62-63 are time integrated for the positions of the cytoskeletal network and membrane/cortex structure and Eq. 35 for the reference configuration of the cytoskeletal network using the Runge-Kutta-Fehlberg method, order 4/5 with a variable time step. In these simulations, the cell membrane can be very close to the channel wall. The high time accuracy with error control makes it less likely for the membrane to cross the channel wall due to time integration error. Given the parameters in Table 1 and a relative tolerance of 10^{-3} for the Runge-Kutta method, the resulting temporal discretisation has an average time step of $\Delta t = 5.53 \times 10^{-4}$ minutes. Model parameters are discussed below and provided in Table 1.

Model parameters. We perform simulations using the parameter values listed in Table 1. The cytoskeletal relaxation timescale, λ_T , is the only parameter varied to produce the different cytoskeleton material models in Fig. 9. Where possible, parameter values are chosen to be roughly the same order of magnitude as measured or estimated values in literature. The viscous drag coefficient is given by the ratio of the dynamic viscosity of the fluid and the cytoplasmic permeability, $\xi = \mu/\kappa$.

Symbol	Quantity	Value
R_0	Resting radius	$8.0~\mu\mathrm{m}$
γ	Resting tension for membrane-cortex link	$400~\mathrm{pN}/\mu\mathrm{m}$
k	Elastic stiffness for membrane-cortex link	$1600~\mathrm{pN}/\mu\mathrm{m}$
G	Cytoskeletal shear modulus	142.5 Pa
K	Cytoskeletal bulk modulus	285 Pa
λ_T	Cytoskeletal relaxation timescale	2 - 17 mins
μ	Cytosolic fluid viscosity	0.5 Pa⋅s
κ	Cytoplasmic permeability	$0.0067~\mu{\rm m}^2$
ΔP	Prescribed pressure drop	190 Pa
2R	Vertical separation between horizontal walls of channel	44 $\mu \mathrm{m}$
w	Width of the narrow channel	$12.6~\mu\mathrm{m}$
$k_{\text{repulsive}}$	Constant for cell-surface repulsive interaction	19 kPa
δ_w	Cell-to-wall separation distance	$0.05~\mu\mathrm{m}$

Table 1: Definition and values of parameters for a cell passing through a microfluidic channel simulation.

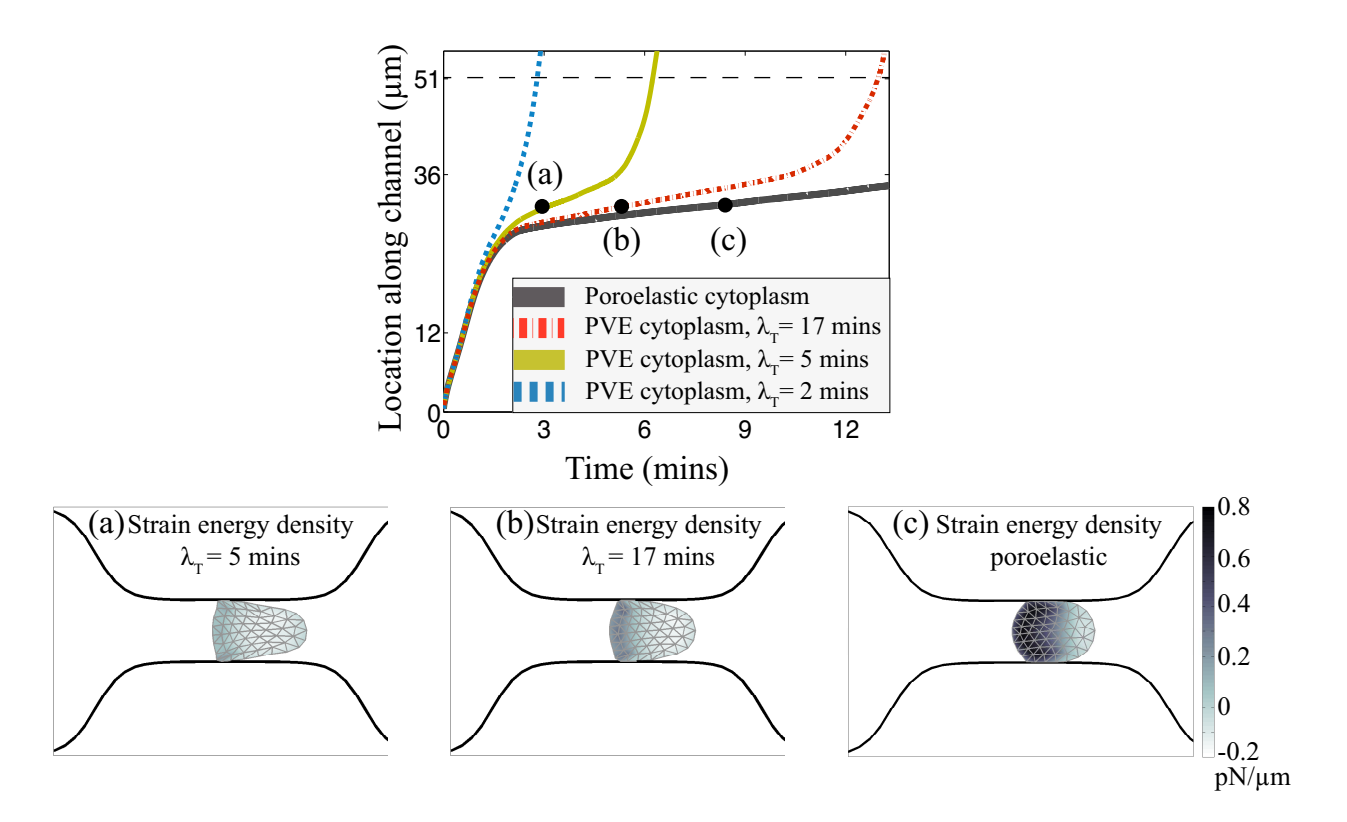


Figure 9: Transit time through a microfluidic channel for a cell with different rheological descriptions of the cytoskeleton. The location of the rear of the cell is plotted as a function of time for the two cytoplasm models: poroelastic (solid, grey line) and poro-viscoelastic material with various relaxation timescales. The dashed, black line indicates the end of the narrow portion of the channel at 51 μ m. The subplots represent snapshots of the cell's position in the microfluidic channel and its corresponding strain energy density throughout the structure for different cytoskeleton models, at different times but at the same location in the channel. Positive strain energy density indicates a compression of the material, while a negative strain energy density indicates expansion. The thickness of the gap between the cell membrane and the channel walls determines the resistance to movement of the cell through the channel due to a prescribed pressure gradient. For the poroelastic cytoskeleton, the outward elastic forces push the cell toward the channel walls resulting in a small gap size (panel c). In the case of the porous viscoelastic cytoskeleton, the restoring forces decay in time forming a larger gap size (panel a) which offers less shear effective friction as the cell moves through the channel.

4.4 The effects of the cell cytoplasm rheology for confined fluid-driven locomotion

As the cell is driven by fluid flow through the microfluidic channel, the cell position is tracked over time and the time to travel the length of the tube is recorded for the different cytoskeleton material models (Fig. 9). Given the current and reference configuration of the structure, the strain energy density of the material is also computed every time step by the constitutive relation for a compressible neo-Hookean material in Eq. 9. We note that the cells are not adhering to the surface of the channel

but instead interact with the surface of the channel through steric forces and are solely driven by extracellular fluid flow arising from the prescribed pressure difference. For the different simulations all parameters were kept constant except for the relaxation modulus for the actin cytoskeleton, λ_T , which was varied to be either 2, 5 or 17 minutes. If we consider a cell speed of $10~\mu\text{m/min}$ (varies due to the cell type and flow conditions) and a channel length of $51~\mu\text{m}$, the time to traverse the channel is 5 minutes. The different values for the relaxation timescale were chosen relative to the travel time for a characteristic cell speed of $10~\mu\text{m/min}$.

In the case of the poroelastic cytoskeleton (solid, grey line in Fig. 9), as the cell travels through the channel it gets constricted and deformed, and consequently its strain energy density increases due to the deformation as shown in Fig. 9c. As the cell passes through the channel, the cell speed is partially determined by the gap between the channel and the cell membrane. The thickness of the gap is the result of a balance between pressure and the outward normal forces due to the elasticity of the cytoskeleton. For the poroelastic cytoskeleton, the elastic forces push in the outward normal direction creating a smaller space and thus, more resistance to the forward motion. Thus, the cell moves slowly across the channel and its transit time is approximately 30 minutes. However, in the case of the porous viscoelastic cytoskeleton, the restoring elastic force decays in time which allows for larger gaps between the cell membrane and channel walls, and lowers the frictional resistance to forward motion. In particular, we observe that as the relaxation timescale decreases, the transit time through the narrow channel decreases as shown in Fig. 9. For example, for a relaxation timescales of 2 minutes, which is roughly the timescale for reorganisation of actin filaments in the cytoskeleton, the transit time is an order of magnitude smaller than in the case of a poroelastic cytoplasm. We attribute a faster passage time to a decrease in the material's elastic resistance against the channel walls. Indeed, if we compare the cell's strain energy density at the same location in the channel but for different cytoskeletal models (Fig. 9a-c), we find that as the relaxation timescale decreases so does the strain energy density function across the cell. This decrease in the strain energy is caused by the material forgetting its original configuration, and thus the network offers less resistance against the channel walls and allows for a faster transit time. We find that the rheology of the cytoskeleton has a substantial effect on the passage time through a microfluidic channel, and thus, this model provides the appropriate framework to capture the effects of cytoplasmic rheology and cytoskeletal reorganisation for confined cell motility. We note that the interaction between the cell and the channel wall presented in Fig. 9, occurs on lengthscales that are on or below the mesh spacing. While this interaction is not well resolved, we have found that with finer resolution, the phenomenon of longer transit time for the poroelastic cytoskeleton than the porous viscoelastic cytoskeleton is a generic result of the problem. However, resolving the boundary layer of this cell-surface interaction and getting the interaction quantitatively right would require either a higher spatial resolution or a more detailed model of the cell-wall interaction.

5 Conclusions

In this paper, we presented a method for simulating porous viscoelastic material immersed in viscous fluid. This method is based on the poroelastic IB method [30] in which the fluid and the structure phase move with their own velocity field and the two phases are coupled through drag forces. Because the structure and the fluid mechanics can be decoupled at each time step, fast methods for solving the equations of the fluid mechanics can be used. Given that the material quantities are more naturally represented in a Lagrangian framework, we developed a model for viscoelasticity in a moving frame

that in the limit of infinitesimal strain is analogous to the linearised Maxwell model. However, the viscoelasticity model presented here is non-linear and valid for large deformations that are common in biological problems. As shown in Section 3.1, the network with a time-evolution equation for the reference configuration mechanically, behaved like a linear viscoelastic material for small deformations. In Section 3.2, we validated that dynamically the network's response matched that of a porous viscoelastic material permeated by an incompressible viscous fluid.

The model of a viscoelastic material in this work is an extension of our poroelastic immersed boundary method [30], where the material's elastic forces are computed using a variational derivative of the energy. The method begins with a continuum expression for viscoelasticity to derive an ordinary differential equation for the relaxation of the material's reference configuration. Hence, the formulation resembles the mixed Eulerian-Lagrangian methods [11, 14] in that a continuum expression for viscoelasticity underlies the numerical method. However, instead of transforming elastic quantities back and forth between the Eulerian and Lagrangian frames, we exploit the fact that material quantities are naturally represented in a Lagrangian coordinate system and compute viscoelasticity on a moving, deforming frame. One advantage of this method over simply using a continuum viscoelastic model, is that stress relaxation is imposed through a simple ordinary differential equation on the material. Although only two-dimensional problems are considered in this paper, extending the method to three-dimensional materials is trivial.

The viscoelastic model presented here is developed from a continuum description, but another approach is to describe the material as a network composed of discrete viscoelastic elements as done by Wróbel et al. [34]. However, there are several limitations of spring-based models of elasticity [30]. Specifically, in the spring model it is not clear what constitutive laws are modelled for the large deformations and moreover, the mechanical properties of the material depend on the structure of the mesh. The energy-based elasticity models do not have the limitations of the spring-based model, and in our tests, the energy-based elasticity method was found to be much more accurate [30]. Here, we exploit the fact that the first Piola-Kirchhoff stress tensor appears in the energy-based computation of elasticity and we derive viscoelasticity for this stress tensor. Another advantage of this formulation is the ability to include isotropic or anisotropic compressive and extensile (swelling) stresses in the method. For example, including anisotropic swelling stresses in the method could be used to simulate the formation of actin-rich protrusions such as filopodia and lamellipodia. However, in this case, to prevent artefacts in the local material properties of the network due to mesh distortion, a model for local conservation of actin density will be necessary. In particular, the method does not guarantee to preserve the mesh spacing as the material deforms in the case of large strain and small relaxation modulus as shown in Fig. 10. This is due to the fact that the model for viscoelasticity describes a fluid rather than solid as in the poroelastic immersed boundary method [30], and in such cases, re-meshing algorithms will need to be incorporated in the framework [3, 15].

This work was motivated by problems in cell biology, and our results showed that porous viscoelastic models were essential to describe the dynamics in the system presented. However, the modelling framework and methods are not limited to applications in cell biology. Porous structures can be found in many contexts in biology and engineering, and our models could be adapted to these problems.

Acknowledgments The authors thank W. Strychalski for helpful comments. This work was supported in part by NSF grant DMS-1664679 to R.D.G. Additionally, C.C. was supported by NSF grant DGE-1148897.

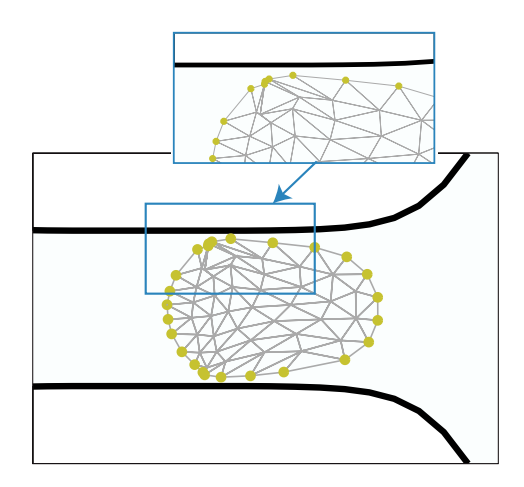


Figure 10: **Mesh distortion due to motion with large deformations.** Since in the limit of small relaxation timescale, the constitutive law for viscoelasticity describes a viscous fluid, the method does not guarantee to preserve the mesh spacing as the material deforms. Thus, for large deformations, in the case of moving, deforming structure, re-meshing algorithms need to be considered.

References

- [1] W. Alt and M. Dembo. Cytoplasm dynamics and cell motion: two-phase flow models. <u>Math.</u> <u>Biosci.</u>, 156:207–228, 1999.
- [2] M. A. Biot. General theory of three-dimensional consolidation. <u>J. Appl. Phys.</u>, 12:155–164, 1941.
- [3] H. Borouchaki, P. L. George, F. Hecht, P. Laug, and E. Saltel. Delaunay mesh generation governed by metric specifications. Part I: Agorithms.
- [4] B. S. Cho, T. G. Schuster, X. Zhu, D. Chang, G. D. Smith, and S. Takayama. Passively driven integrated microfluidic system for separation of motile sperm. <u>Anal. Chem.</u>, 75:1671–1675, 2003.
- [5] N. G. Cogan and R. D. Guy. Multiphase flow models of biogels from crawling cells to bacterial biofilms. HFSP J., 4:11–25, 2010.
- [6] R. Cortez. The method of regularized Stokeslets. SIAM J. Sci. Comput., 23:1204–1225, 2001.
- [7] R. Cortez, N. Cowen, L. Fauci, and R. Dillion. Simulation of swimming organisms: coupling internal mechanics with external fluid dynamics. <u>Comp. Sci. & Eng.</u>, 6:38–45, 2004.
- [8] D. Devendran and C. S. Peskin. An immersed boundary energy-based method for incompressible viscoelasticity. J. Comput. Phys., 231:4613–4642, 2012.
- [9] R. Dillion and L. Fauci. An integrative model of internal axoneme mechanics and external fluid dynamics in ciliary beating. J. Theor. Biol., 207:415–430, 2000.
- [10] R. Dillion, L. Fauci, A. Fogelson, and D. Gaver. Modeling biofilm processes using the immersed boundary method. J. Comp. Phys., 129:57–73, 1996.

- [11] J. Étienne, E. J. Hinch, and J. Li. A Lagrangian-Eulerian approach for the numerical simulation of free-surface flow of a viscoelastic material. <u>J. Non-Newtonian Fluid Mech</u>, 136:157–166, 2006.
- [12] M. L. Gardel, K. E. Kasza, C. P. Brangwyne, J. Liu, and D. A. Weitz. Mechanical response of cytoskeletal networks. Methods Cell Biol., 89:487–519, 2008.
- [13] M. Gracheva and H. Othmer. A continuum model of motility in ameboid cells. <u>Bull. Math.</u> Biol., 66:167–193, 2004.
- [14] O. G. Harlen, J. M. Rallison, and P. Szabo. A split Lagrangian-Eulerian method for simulating transient viscoelastic flows. J. Non-Newtonian Fluid Mech, 60:81–104, 1995.
- [15] F. Hecht. bamg: Bidimensional anisotropic mesh generator. Technical report, INRIA, Rocquencourt, France, 1997.
- [16] M. L. Heuzé, O. Collin, E. Terriac, A. M. Lennon-Duménil, and M. Piel. Cell migration in confinement: A micro-channel-based assay. In A. Ridley, M. Peckham, and P. Clark, editors, <u>Cell Migration</u>. <u>Methods in Molecular Biology (Methods and Protocols)</u>, pages 415–434. Humana Press, 2011.
- [17] D. D. Joseph. <u>Fluid dynamics of viscoelastic liquids</u>. Springer-Verlag, New York, 1st edition, 1990.
- [18] A. J. Levine and F. C. MacKintosh. The mechanics and fluctuation spectrum of active gels. <u>J. Phys. Chem.</u>, 113:3820–3820, 2009.
- [19] O. L. Lewis, S. Zhang, R. D. Guy, and J. C. del Álamo. Coordination of contractility, adhesion and flow in migrating *Physarum* amoebae. J. R. Soc. Interface, 12:1–12, 2015.
- [20] L. E. Malvern. <u>Introduction to the mechanics of a continuous medium</u>. Prentice Hall, New York, 1st edition, 1977.
- [21] K. Matrin, T. Henkel, A. Grodrian, T. Schön, M. Roth, J. M. Köhler, and J. Metze. Generation of larger numbers of separated microbial populations by cultivation in segmented-flow microdevices. <u>Lab Chip</u>, 3:202–207, 2003.
- [22] T. J. Mitchison, G. T. Charras, and L. Mahadevan. Implications of a poroelastic cytoplasm for the dynamics of animal cell shape. <u>Semin. Cell Dev. Biol.</u>, 19:215–223, 2008.
- [23] M. R. K. Mofrad. Rheology of the cytoskeleton. Annu. Rev. Fluid Mech., 41:433–453, 2009.
- [24] S. Nam, K. H. Hu, M. J. Butte, and O. Chaudhuri. Strain-enhanced stress relaxation impacts nonlinear elasticity in collagen gels. Proc. Natl. Acad. Sci. USA., 113:5492–5497, 2016.
- [25] P. Persson and G. Strang. A simple mesh generator in Matlab. <u>SIAM Rev.</u>, 46:329–345, 2004.
- [26] C. S. Peskin. Numerical analysis of blood flow in the heart. <u>J. Comput. Phys.</u>, 25:220–252, 1977.

- [27] W. J. Polacheck, J. L Charest, and R. D. Kamm. Interstitial flow influences direction of tumor cell migration through competing mechanisms. Proc. Natl. Acad. Sci. USA., 108:11115–11120, 2011.
- [28] J. P. Shelby, J. White, K. Ganesan, P. K. Rathod, and D. T. Chiu. A microfluidic model for single-cell capillary obstruction by *Plasmodium falciparum* infected erythrocytes. <u>Proc. Natl.</u> Acad. Sci. USA., 100:14618–14622, 2003.
- [29] S. Sonam, S. R. Sathe, E. K. F. Yim, M. P. Sheetz, and C. T. Lim. Cell contractility arising from topography and shear flow determines human mesenchymal stem cell fate. <u>Sci. Rep.</u>, 6:1–12, 2016.
- [30] W. Strychalski, C. A. Copos, O. L. Lewis, and R. D. Guy. A poroelastic immersed boundary method with applications to cell biology. J. Comp. Phys., 282:77–97, 2015.
- [31] W. Strychalski and R. D. Guy. Intracellular pressure dynamics in blebbing cells. <u>Biophys. J.</u>, 110:1168–1179, 2016.
- [32] G. M. Whitesides. The origins and the future of microfluidics. Nature, 442:368–373, 2006.
- [33] G. M. Whitesides, E. Ostuni, S. Takayama, X. Jiang, and D. E. Ingber. Soft lithography in biology and biochemistry. Annu. Rev. Biomed. Eng., 3:335–373, 2001.
- [34] J. K. Wróbel, L. Fauci, and R. Cortez. Modeling viscoelastic networks in Stokes flow. Phys. Fluids, 11:113102, 2014.

A Solution to the linearized Maxwell model for a linear expansion

In this appendix, we derive an expression for the network velocity due to a prescribed deformation for a porous viscoelastic material with a simple constitutive law,

$$\sigma = G\mathcal{A}\mathcal{A}^T, \tag{A.1}$$

where G denotes an elastic modulus. We consider a dynamical test where the motion of the outer boundary of a circular viscoelastic structure of radius R is prescribed to move in the outward normal direction with velocity, U_0 . In this case, the fluid velocity is zero, and the system in Eqs. 32-33, simplifies to the single equation,

$$\nabla \cdot \sigma - \xi \, \boldsymbol{U} = 0 \,, \tag{A.2}$$

where U denotes the network velocity. The upper-convected Maxwell model for the time-history of the Cauchy stress tensor with relaxation modulus λ_T , is given by,

$$\lambda_T \stackrel{\nabla}{\sigma} + \sigma = GI , \qquad (A.3)$$

where ∇ is the material time derivative of a tensor called the upper convected time derivative,

$$\overset{\nabla}{\sigma} = \frac{\partial \sigma}{\partial t} + \boldsymbol{U} \cdot \nabla \sigma - \nabla \boldsymbol{U} \cdot \sigma - \sigma \cdot \nabla \boldsymbol{U}^{T}. \tag{A.4}$$

To find the solution of the linearised upper-convected Maxwell equation for a linear expansion test, first, we linearise the model equation for viscoelasticity about the equilibrium: $q = 0, U = 0, \sigma = GI$, where q denotes displacement. Note that the network displacement and velocity are related by

$$\frac{\partial \boldsymbol{q}}{\partial t} = \boldsymbol{U} .$$

For a small perturbation about the equilibrium, $\sigma = \tau + GI$, Eq. A.3 yields:

$$\nabla \cdot \tau - \xi \mathbf{U} = 0 \tag{A.5}$$

$$\lambda_T \frac{\partial \tau}{\partial t} + \tau = 2G\lambda_T D , \qquad (A.6)$$

where $D=1/2(\nabla {\pmb U}+\nabla {\pmb U}^T)$ is the rate-of-deformation tensor. Since the deformation is only in the radial direction, the network velocity is

$$U(r,t) = (U_r, U_\theta) = (U_r, 0),$$
 (A.7)

where $U_r = \mathbf{U} \cdot \mathbf{e}_r$ and $U_\theta = \mathbf{U} \cdot \mathbf{e}_\theta$ correspond to the radial and angular components of the velocity. We obtain a dynamic equation for the radial velocity by applying the divergence operator to Eq. A.6 and then combining it with Eq. A.5,

$$\lambda_T \frac{dU_r}{dt} + U_r = \frac{2G\lambda_T}{\xi} \left(\frac{1}{r} \frac{\partial U_r}{\partial r} + \frac{\partial^2 U_r}{\partial r^2} - \frac{1}{r^2} U_r \right). \tag{A.8}$$

Because the material is undergoing a prescribed expansion due to non-zero velocity at the boundary, we take the following boundary condition: $U_r(R,t) = U_0$. Further, we assume that initially the

network experiences no deformation, $U_r(r, 0) = 0$. To find an explicit expression for network velocity, we look for separable solutions of the form $U_r(r, t) = \mathcal{U}(r)\mathcal{T}(t)$:

$$\frac{\xi}{2G\lambda_T} \left(\frac{\lambda_T \dot{\mathcal{T}} + \mathcal{T}}{\mathcal{T}} \right) = \frac{1}{r} \frac{\mathcal{U}'}{\mathcal{U}} + \frac{\mathcal{U}''}{\mathcal{U}} - \frac{1}{r^2} = -c_k^2 , \qquad (A.9)$$

where \bullet denotes a time derivative and c_k^2 are non-zero constants. Then, the network velocity is

$$U_r(r,t) = \sum_{k=1}^{\infty} D_k J_1(c_k r) e^{-(2G\lambda_T c_k^2/\xi + 1)t/\lambda_T} , \qquad (A.10)$$

where J_1 represents the Bessel function of the first kind and D_k are the series coefficients. Because of the non-homogeneous boundary condition, the solution in Eq. A.10 does not satisfy the boundary condition and instead we write the solution to the differential equation with the appropriate boundary conditions as,

$$\widetilde{U_r}(r,t) = U_r(r,t) + V(r) , \qquad (A.11)$$

where U_r solves the differential equation with the homogeneous boundary condition, $U_r(R,t) = 0$, and the initial condition is $U_r(0,r) = 0 - V(r)$ and V is such that it is the steady state solution to Eq. A.8,

$$V = \frac{2G\lambda_T}{\xi} \left(\frac{1}{r} V' + V'' - \frac{1}{r^2} V \right) , \tag{A.12}$$

with $V(1) = U_0$. We find that the solution to the full system is

$$\widetilde{U}_r(r,t) = \sum_{k=1}^{\infty} D_k J_1(c_k r) e^{-(2G\lambda_T c_k^2/\xi + 1)t/\lambda_T} + U_0 \frac{I_1\left(r\sqrt{\frac{\xi}{2G\lambda_T}}\right)}{I_1\left(\sqrt{\frac{\xi}{2G\lambda_T}}\right)}, \tag{A.13}$$

where I_1 is the modified Bessel function of the first kind. From the boundary condition on U_r :

$$U_r(R,t) = 0 \Rightarrow J_1(c_k R) = 0$$
, (A.14)

we find that c_k are the zeros of the Bessel function of the first kind. The initial condition on U_r ,

$$U_r(r,0) = -V(r) \Rightarrow \sum_{k=1}^{\infty} D_k J_1(c_k r) = -U_0 \frac{I_1\left(r\sqrt{\frac{\xi}{2G\lambda_T}}\right)}{I_1\left(\sqrt{\frac{\xi}{2G\lambda_T}}\right)}, \tag{A.15}$$

yields the coefficients of the series expansion

$$D_{k} = -U_{0} \frac{\int_{0}^{1} J_{1}(c_{k}r) \frac{I_{1}\left(r\sqrt{\frac{\xi}{2G\lambda_{T}}}\right)}{I_{1}\left(\sqrt{\frac{\xi}{2G\lambda_{T}}}\right)} r dr}{\int_{0}^{1} J_{1}(c_{k}r) \cdot J_{1}(c_{k}r) r dr},$$
(A.16)

from the orthogonality of the Bessel functions of the first kind in the appropriate inner product,

From the orthogonality of the Bessel functions of the first kind in the appropriate limer product,
$$\langle f,g\rangle = \int_0^1 x \, f(x) \, g(x) \, dx$$
. Thus, the network velocity in the radial direction r and at a particular time t is
$$\widetilde{U_r}(r,t) = \sum_{k=1}^\infty D_k \, J_1(c_k r) e^{-(2G\lambda_T c_k^2/\xi + 1)t/\lambda_T} + U_0 \frac{I_1\left(r\sqrt{\frac{\xi}{2G\lambda_T}}\right)}{I_1\left(\sqrt{\frac{\xi}{2G\lambda_T}}\right)}, \tag{A.17}$$

where c_k denotes the zeros of the Bessel function of the first kind, D_k are the coefficients provided in Eq. A.16, and U_0 represents the prescribed velocity at the boundary of the material.